J. Fluid Mech. (2009), *vol.* 628, *pp.* 357–369. © 2009 Cambridge University Press
doi:10.1017/S0022112009006673 Printed in the United Kingdom

Origin of transonic buffet on aerofoils

J. D. CROUCH[1]†, A. GARBARUK[2], D. MAGIDOV[2] AND A. TRAVIN[2]

[1]The Boeing Company, Seattle, WA 98124-2207, USA

[2]Saint Petersburg Polytechnic University, St Petersburg, 195251 Russia

(Received 14 August 2008 and in revised form 20 February 2009)

Buffeting flow on transonic aerofoils serves as a model problem for the more complex three-dimensional flows responsible for aeroplane buffet. The origins of transonic aerofoil buffet are linked to a global instability, which leads to shock oscillations and dramatic lift fluctuations. The problem is analysed using the Reynolds-averaged Navier–Stokes equations, which for the foreseeable future are a necessary approximation to cover the high Reynolds numbers at which transonic buffet occurs. These equations have been shown to reproduce the key physics of transonic aerofoil flows. Results from global-stability analysis are shown to be in good agreement with experiments and numerical simulations. The stability boundary, as a function of the Mach number and angle of attack, consists of an upper and a lower branch – the lower branch shows features consistent with a supercritical bifurcation. The unstable modes provide insight into the basic character of buffeting flow at near-critical conditions and are consistent with fully nonlinear simulations. The results provide further evidence linking the transonic buffet onset to a global instability.

1. Introduction

Transonic buffet is characterized by large-scale lift oscillations that can limit the flight envelope of aircraft. This generally occurs at the higher lift coefficients associated with higher-altitude flight. Many of the features observed in aeroplane buffet are also observed in the unsteady flow fields of transonic aerofoils. Starting at a moderate lift coefficient, as the angle of attack is increased the shock intensifies and moves aft over the aerofoil. At sufficiently high angles of attack, the boundary layer separates – either as a bubble at the foot of the shock or at the trailing edge. Further increases in the angle of attack often lead to separation at the shock, extending to the trailing edge. At some point in this process, the flow can become highly unsteady with large oscillations in the shock position leading to large lift fluctuations.

The practical problem of aeroplane buffet results from a structural response to the buffeting flow field. Predictions of aeroplane buffet are often highly empirical, attempting to link different features of the flow field with measured accelerations of the aeroplane structure. Meanwhile, the prediction of the onset and character of the unsteady flow field is itself a great challenge. The transonic aerofoil has been used as a model problem for understanding the unsteady forcing, since it exhibits features similar to the aeroplane buffeting response. Controlled experiments show a fairly sudden onset of flow unsteadiness as the angle of attack is increased (McDevitt &

† Email address for correspondence: jeffrey.d.crouch@boeing.com

Okuno 1985; Jacquin *et al.* 2005). This is characterized by large pressure fluctuations near, and downstream of, the shock.

A number of empirical criteria have been proposed for predicting the onset of buffeting flow (see, for example, the review of Lee 2001). These are linked to heuristic models, which describe the structure of the buffeting flow field. One of the simplest of these criteria is based only on a threshold for the pre-shock Mach number. Other models consider zones of separation and how these vary with changes in the shock strength or position. While some of these models provide useful descriptors for the flow behaviour, they have not been effective as predictors for the buffet onset. Lee (2001) notes in his review that even though the buffet problem has been known for 50 years, the physical mechanism for buffet onset is still not fully understood.

Meanwhile, Crouch, Garbaruk & Magidov (2007, hereafter CGM) have linked the origins of aerofoil buffet onset to a global instability of the underlying flow field. The stability theory effectively predicts the initial buffet boundary (Crouch *et al.* 2007, 2009) and the structure of the buffeting velocity field (Crouch *et al.* 2009). Here we make use of a combination of global-stability theory and unsteady Reynolds-averaged Navier–Stokes (URANS) simulations to further explore the origins of transonic buffet and to assess existing empirical and mechanistic descriptors and predictors for buffet onset. Results are presented to illuminate the basic character of the global-instability bifurcation and to more fully map the stability boundary at higher Mach numbers.

2. Global-stability theory

Global-stability theory has been used to analyse a wide variety of low-speed laminar flows, as reviewed by Theofilis (2003). Here we follow the formulation of CGM, which accounts for high Reynolds numbers and compressible flow. We consider two-dimensional transonic flow, with chord Reynolds numbers of $Re_c = O(10^7)$. At these Reynolds numbers, much of the viscous shear-layer flow is turbulent. However, in the current study we are interested in time scales much longer than the characteristic eddy time scales. Thus, we employ the URANS equations, where the large-scale unsteadiness is explicit, but the effects of the turbulence fluctuations in the shear layers are modelled to provide closure for the averaged Reynolds stresses (see § 3 for more details). The turbulence model used is the compressible form of the Spalart–Allmaras (S-A) model (Spalart & Allmaras 1994) – including the compressibility correction (Spalart 2000). Here, we focus on flows that can be treated as either laminar or 'fully turbulent', which removes the need for the trip-term functions. This leads to a set of five equations: continuity, streamwise momentum, transverse momentum, energy and modified eddy-viscosity equations. These equations can be written in terms of the primitive variables $\boldsymbol{q} = \{\rho, u, v, T, \tilde{\nu}\}$ as follows:

$$\frac{\partial}{\partial t} M[\boldsymbol{q}] + Q[\boldsymbol{q}] + N[\boldsymbol{q}, \boldsymbol{q}] = 0, \tag{1}$$

where M and Q are linear operators and N contains all nonlinear terms.

The boundary conditions imposed on the surface of the body are

$$\left.\begin{aligned} &u = v = 0, \\ &\frac{\partial \rho}{\partial n} = \frac{\partial T}{\partial n} = 0, \\ &\tilde{\nu} = 0, \end{aligned}\right\} \tag{2}$$

where $\partial/\partial n$ is a derivative normal to the surface, and the density condition is derived from the equation of state. The far-field conditions used in the compressible

computations involve not only the primary variables $\rho, u, v, T, \tilde{\nu}$ but also the Riemann invariants. These conditions, expressed in terms of the primary variables, are given as

$$\left.\begin{aligned} I_1 &= V_n + \frac{2a}{(\gamma-1)} = k_x u + k_y v + \frac{2}{(\gamma-1)}\sqrt{\gamma RT}, \\ I_2 &= V_n - \frac{2a}{(\gamma-1)} = k_x u + k_y v - \frac{2}{(\gamma-1)}\sqrt{\gamma RT}, \\ I_3 &= V_\tau = k_y u - k_x v, \qquad\qquad I_4 = \frac{RT}{\rho^{\gamma-1}}. \end{aligned}\right\} \tag{3}$$

Here k_x, k_y are the local directional cosines of the boundary normal. These conditions are imposed on the subsonic boundaries in the following way: On the inlet boundary, $\tilde{\nu}$ and invariants I_1, I_3, I_4 are given, and I_2 is extrapolated from the computational domain. On the outlet boundary, $\tilde{\nu}$ and I_1, I_3, I_4 are extrapolated from the computational domain, and I_2 is given.

The state vector describing the total flow field can be decomposed into a steady state $\bar{\boldsymbol{q}} = \{\bar{\rho}, \bar{u}, \bar{v}, \bar{T}, \bar{\tilde{\nu}}\}$ and an unsteady vector $\boldsymbol{q}' = \{\rho', u', v', T', \tilde{\nu}'\}$, $\boldsymbol{q} = \bar{\boldsymbol{q}} + \boldsymbol{q}'$. The vector $\bar{\boldsymbol{q}}$ is a solution to the steady form of (1)–(3) – that is with $\partial\bar{\boldsymbol{q}}/\partial t \equiv 0$. The steady-state RANS equations are normally rewritten in conservative form before being solved numerically. For conditions close to steady state, the unsteady component $\boldsymbol{q}'$ can be considered a small perturbation to the vector $\bar{\boldsymbol{q}}$. Substituting $\boldsymbol{q} = \bar{\boldsymbol{q}} + \boldsymbol{q}'$ into (1), cancelling the terms governing $\bar{\boldsymbol{q}}$ and linearizing the equations in terms of $\boldsymbol{q}'$ yields

$$\frac{\partial}{\partial t} M[\boldsymbol{q}'] + N_{\bar{q}}[\boldsymbol{q}'] = 0. \tag{4}$$

The linear operator M contains the terms associated with the time derivatives from the original equation (1). The linear operator $N_{\bar{q}}$ consists of linear terms from the original equations and the terms generated by nonlinear interactions between $\bar{\boldsymbol{q}}$ and $\boldsymbol{q}'$.

The unsteady perturbation to the steady-state flow $\bar{\boldsymbol{q}}(x, y)$ can be represented by time-harmonic modes of the form

$$\boldsymbol{q}'(x, y, t) = \hat{\boldsymbol{q}}(x, y) \cdot \exp(-\mathrm{i}\omega t). \tag{5}$$

The function $\hat{\boldsymbol{q}}$ describes the mode shape, and ω is the frequency. In general, both $\hat{\boldsymbol{q}}$ and ω can be complex, so the physical solution is taken as the real part of (5). Substituting (5) into (4) and rescaling the terms yields a system of equations for $\hat{\boldsymbol{q}}$ and ω:

$$-\mathrm{i}\omega\hat{\boldsymbol{q}} + L(\bar{\boldsymbol{q}}) \cdot \hat{\boldsymbol{q}} = 0, \tag{6}$$

with L being a second-order differential operator.

The boundary and far-field conditions are obtained by introducing $\boldsymbol{q} = \bar{\boldsymbol{q}} + \boldsymbol{q}'$ into the expressions (2) and (3), cancelling the terms governing the steady state and linearizing with respect to $\boldsymbol{q}'$. Then substituting (5) for $\boldsymbol{q}'$ yields the boundary conditions for $\hat{\boldsymbol{q}}$:

$$\left.\begin{aligned} &\hat{u} = \hat{v} = 0, \\ &\frac{\partial\hat{\rho}}{\partial n} = \frac{\partial\hat{T}}{\partial n} = 0, \\ &\hat{\tilde{\nu}} = 0. \end{aligned}\right\} \tag{7}$$

The far-field conditions for the inlet boundary are given by

$$\left.\begin{aligned} &\hat{I}_1 = \hat{I}_3 = \hat{I}_4 = \hat{\tilde{\nu}} = 0, \\ &\frac{\partial \hat{I}_2}{\partial n} = 0, \end{aligned}\right\} \tag{8}$$

and for the outlet boundary

$$\left.\begin{aligned} &\frac{\partial \hat{I}_1}{\partial n} = \frac{\partial \hat{I}_3}{\partial n} = \frac{\partial \hat{I}_4}{\partial n} = \frac{\partial \hat{\tilde{\nu}}}{\partial n} = 0, \\ &\hat{I}_2 = 0. \end{aligned}\right\} \tag{9}$$

The variables $\hat{I}_1$, $\hat{I}_2$, $\hat{I}_3$ and $\hat{I}_4$ are the linearized versions of the Riemann invariants (see (3)). Additional details are given in CGM. Equations (6)–(9) describe an eigenvalue problem governing the complex frequency ω and mode shape $\hat{\boldsymbol{q}}$.

3. RANS, URANS and eigenmode analysis of transonic aerofoils

The dominant features of the turbulent flow over a transonic aerofoil, even at flow conditions before buffet onset, include a strong adverse pressure gradient, shock-boundary layer interaction and shock-induced separation. This makes an accurate prediction of such flows in the framework of RANS modelling a severe challenge for turbulence models. Nonetheless, at least some of the contemporary turbulence models are shown to be reasonably successful in terms of acceptable agreement with experiments (e.g. S-A model with the compressibility correction Spalart 2000 used in the present work and k–ω shear-stress transport model of Menter 1994). The RANS calculations predict the major flow parameters, such as shock location, extent of the separation zone, pressure recovery downstream of the shock and pressure in the trailing-edge zone. This has been demonstrated in numerous studies (see, e.g., Catalano & Amato 2003; Garbaruk *et al.* 2003; Bigarella & Azevedo 2007). Thus, there is strong evidence in favour of some RANS models' capability for capturing major transonic-aerofoil flow physics.

For RANS application to transonic-aerofoil flows at buffeting conditions, the experience accumulated is far more limited. Moreover, generally speaking, using the RANS equations in the unsteady mode (URANS approach) does not have a rigorous theoretical background (see e.g. Shur *et al.* 2005; Israel 2006). However, unlike inherently unsteady turbulent flows, the periodic motion of the shock that is a key feature of buffet phenomenon occurs at very low frequencies (non-dimensional frequency $fc/U \ll 1$). Therefore, there is a wide gap between the high frequencies of attached-shear-layer turbulence and the global unsteadiness characteristic of buffet. This justifies using the URANS approach for prediction of transonic buffet on aerofoils assuming that the unsteady mean flow is resolved and that the near wall turbulence is successfully modelled by the same turbulence models shown to be applicable for steady transonic aerofoils with shock-induced separation. This conjecture is supported by the recent studies of Thiery & Coustols (2006) and CGM and gets an additional confirmation in the present work. Note that modelling transonic buffet as a low-Reynolds-number laminar flow would introduce much greater levels of approximation and is unlikely to be effective for investigating this phenomena. A laminar boundary layer would alter the shock location and would transition to turbulence or experience massive separation when going through the shock.

Both the RANS and URANS computations are performed using the New Technologies and Services (NTS) code (Strelets 2001), which is based on an implicit

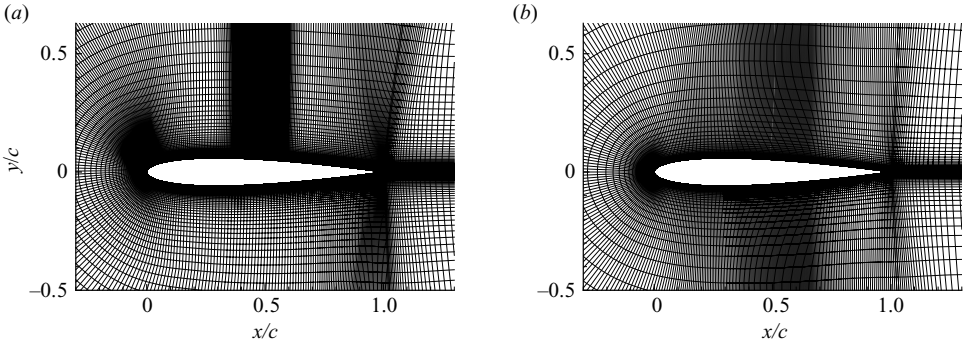

FIGURE 1. Typical two-block grids used for the (*a*) RANS/stability analysis and (*b*) the URANS analysis. Block 1 grid size is 455 × 145 in (*a*) and 403 × 97 in (*b*).

finite-volume formulation on a structured multi-block overlapping grid. A third-order Roe (1981) scheme is used for the inviscid fluxes, and a second-order central difference scheme is used for the viscous momentum and heat fluxes. The convective terms in the turbulence-model equation are approximated using a first-order upwind scheme. In the URANS calculations, the time derivatives are approximated with second-order backward differences (three-layer scheme) with sub-iterations. The code has been exercised for more than 10 years and is proven to be rather accurate and reliable in both RANS and hybrid, RANS/large eddy simulation (RANS/LES), applications.

The eigenvalue problem is also numerically solved using finite differencing. Similar to the steady base flow, upwind differencing is needed to prevent oscillations from the shock. In order to reduce the numerical dissipation of the upwind differencing, we use a 'hybrid' scheme for the stability equations, as in CGM. This is weighted between upwind and central differencing:

$$\Delta_H = \alpha_H \Delta_{3u} + (1 - \alpha_H)\Delta_{4c}, \quad 0 \leqslant \alpha_H \leqslant 1. \tag{10}$$

The finite-difference operators Δ_{3u} and Δ_{4c} correspond to the third-order upwind and fourth-order centred schemes respectively, and α_H is the weighting constant. The influence of the weighting constant is considered in CGM; the current results are based on $\alpha_H = 0.2$. For the stability equations, the upwind finite-differencing approximations are linear.

The steady base flow and the stability equations are solved on the same grid. Typical grids used in the presented results are shown in figure 1. The grid of figure 1(*a*) is used for the RANS and stability calculations. The grid is highly refined in the neighbourhood of the shock, with local streamwise grid spacing of $\Delta x_s = O(0.001c)$. Most of the presented URANS results are based on the grid of figure 1(*b*). However, the grid of figure 1(*a*) and other grids (both coarser and finer resolutions) were also used in the URANS calculations when testing for grid sensitivity.

The discretized eigenvalue problem results in a matrix of dimension $O(100000)$, which is solved using the implicitly restarted Arnoldi method (Lehoucq, Sorensen & Yang 1998). Prior to solution, a spectral transformation is used to transform the eigenvalues in the neighbourhood of ω^* into extreme values for the system. This is achieved using the ARPACK routines (Lehoucq *et al.* 1998) with the shift–invert mode. The value of the prescribed frequency ω_r^* is chosen based on experimental data, where available, or based on the basic model scaling. The prescribed growth rate ω_i^* is taken to be positive. By varying the prescribed frequency, a search can be

made for all unstable modes over a given range. Instability, signifying the onset of unsteadiness, occurs when $\omega_i > 0$.

An unsteady perturbation to a flow field containing a shock will have a large response at the shock location. As a shock is better resolved it becomes thinner, and the unsteady response takes the form of a delta function. A typical steady-flow solution captures the shock over two or three grid points. A linear perturbation to this flow field will exhibit 'ringing' in the neighbourhood of the shock unless some form of shock smoothing is done. The ringing due to the shock will contaminate the eigenfunction and may alter the eigenvalue. To address this, we perform a two-step shock smoothing after the steady flow is calculated. First, the original solution to the steady RANS equations is smoothed over the entire computational domain, resulting in a smoothed field $\bar{\boldsymbol{q}}_{smooth}$. The smoothing is preformed in the dominant flow direction over N_{SC} smoothing cycles. During each cycle, the flow variables are modified according to

$$\bar{\boldsymbol{q}}(i, j) \;=\; \bar{\boldsymbol{q}}(i, j) \;+\; 0.5\, c_i\, [\bar{\boldsymbol{q}}(i+1, j) - 2\bar{\boldsymbol{q}}(i, j) + \bar{\boldsymbol{q}}(i-1, j)], \tag{11}$$

where c_i is a smoothing coefficient that controls the amount of smoothing per cycle. The field $\bar{\boldsymbol{q}}_{smooth}$ is defined by the value of $\bar{\boldsymbol{q}}$ after N_{SC} smoothing cycles. For all of the results presented in this paper, $c_i = 0.1$. In the second step, the smoothed field is blended with the original field in the neighbourhood of the shock, where the grid spacing is very fine; away from the shock, $\bar{\boldsymbol{q}}$ is given by the original field.

4. Buffet onset

To examine the origins of buffet, we focus on the NACA0012 aerofoil as considered in the experiments of McDevitt & Okuno (1985). The experiments show an onset of buffeting flow as the angle of attack is increased at a fixed Mach number. Subsequently, the level of unsteadiness, as measured by surface pressure, increases with the angle of attack. Mach contours from RANS calculations at angles of attack just below the buffet onset are qualitatively similar for different Mach numbers, showing a relatively strong shock followed by a dramatically thickened boundary layer. Near buffet onset, the Mach numbers just before the shock are $M_1 = 1.42$, 1.40 and 1.38 for the free-stream Mach numbers $M = 0.72$, 0.76 and 0.80, respectively. The value M_1 does not provide an obvious indicator for the buffet onset, although the general levels fall between the $M_1 = 1.34$ (observed on the biconvex aierofoil; Mabey, Welsh & Cripps 1981) and $M_1 \approx 1.42$–1.52 (observed on a more conventional wing aerofoil; Lee 1990).

Following the global-stability analysis, the origin of unsteadiness is predicted by the onset of instability. Figure 2 shows the variation of the instability growth rate as a function of angle of attack for $M = 0.76$. The different curves signify different levels of shock smoothing prior to the stability calculation, with $N_{SC} = 0$ corresponding to no smoothing. The buffet onset is predicted to occur at $\alpha \approx 3.02^\circ$ (with $N_{SC} = 80$). In CGM, the smoothing was shown to affect the growth rate due to the change in the shock thickness. Thus, the streamwise grid spacing around the shock also has an influence on the growth rate. For the grid spacing of the curves in figure 2 ($\Delta x_s/c = 0.0015$), the smoothing (with $N_{SC} = 80$) results in a shift of $\alpha = 0.03$ in the buffet onset, as compared to no smoothing. This is considered to be a small source of uncertainty compared to other potential sources, such as nonlinear effects. Grid convergence is demonstrated by the circular symbols, which show the calculated neutral points for different grid spacing near the shock, with fixed $N_{SC} = 80$.

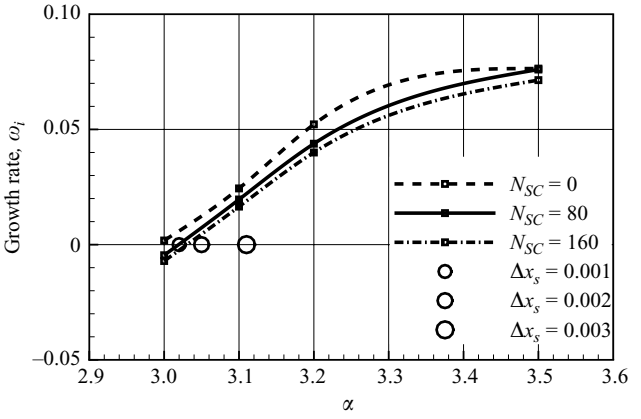

FIGURE 2. Variation of growth rate with aerofoil angle of attack for different levels of smoothing, ($N_{SC} = 0$, 80, 160, with $\Delta x_s/c = 0.0015$), at $M = 0.76$, $Re = 10^7$. Circular symbols show the neutral points calculated with different grid spacing ($\Delta x_s/c = 0.001$, 0.002, 0.003) for $N_{SC} = 80$.

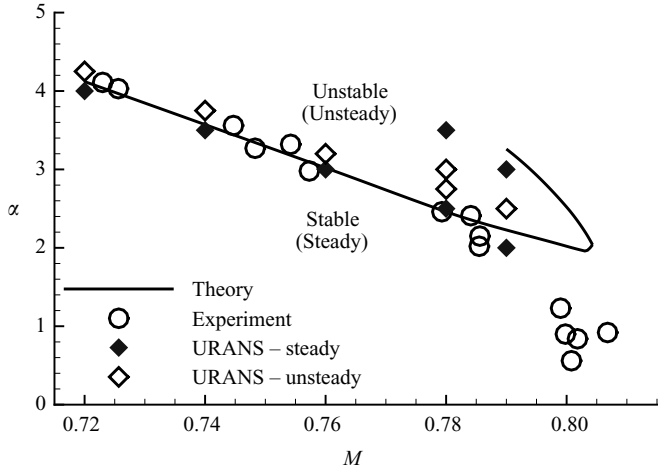

FIGURE 3. Buffet-onset boundary for an NACA0012 aerofoil, with URANS simulation results and experimental data of McDevitt & Okuno (1985); $Re = 10^7$.

The stability boundary is obtained by conducting an analysis similar to that in figure 2 at different free-stream Mach numbers. Figure 3 shows the buffet-onset boundary for the NACA0012 aerofoil. The solid line is the prediction from global-stability theory (with $N_{SC} = 80$), and the open circles are from the experiment of McDevitt & Okuno (1985). Also plotted are results from URANS calculations, where the solid symbols show conditions that remain steady, and the open symbols show conditions that are unsteady; these results are for the grid of figure 1(*b*). The theory, experiment and URANS calculations are all in very good agreement for $M < 0.8$. This good agreement provides evidence for global instability being the cause for transonic-aerofoil buffet onset.

Around $M = 0.8$ the experiment shows an earlier onset of unsteadiness compared to the theory and computations. The stability theory shows significantly smaller growth rates associated with the instability at $M = 0.8$ ($\max[\omega_i] < 0.015$) as compared to

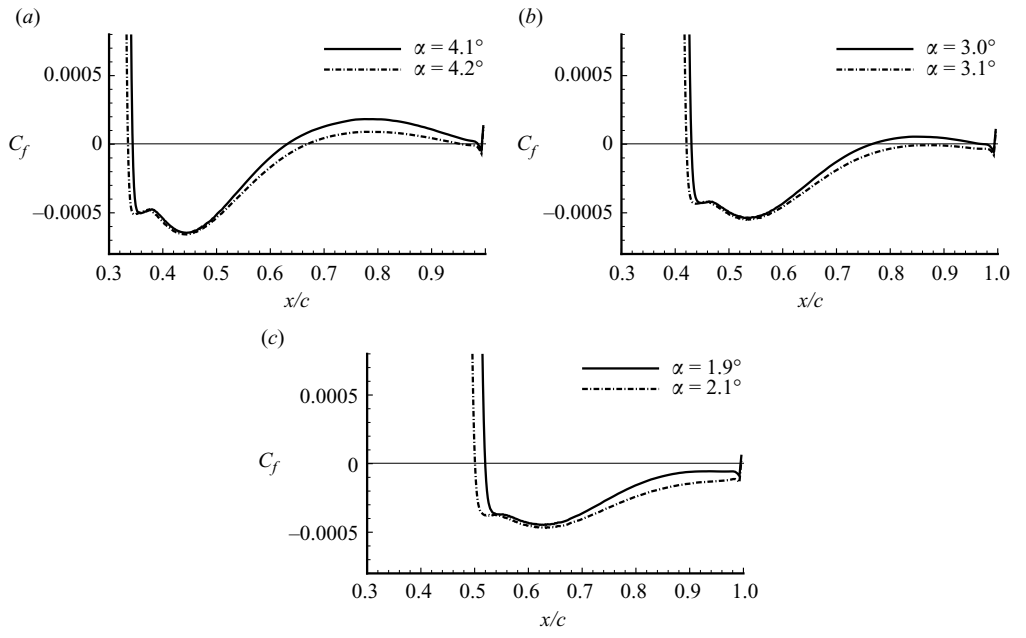

FIGURE 4. Skin-friction coefficient from RANS calculations at angles of attack just below (solid line) and above (dashed line) the predicted buffet onset. NACA0012 aerofoil results at $Re = 10^7$ and (*a*) $M = 0.72$, (*b*) $M = 0.76$ and (*c*) $M = 0.80$.

$M = 0.76$ ($\max[\omega_i] \approx 0.08$). At Mach numbers beyond $M \approx 0.804$, the flow is stable. Below $M \approx 0.804$ there is an upper branch to the stability boundary, signifying that at higher values of α the flow again becomes steady. The URANS approach provides only steady solutions for $M \geqslant 0.8$; this is consistent with the stability results showing small growth rates, which can be damped by numerical dissipation in the time evolution of the URANS equations. URANS simulations on a finer grid (95 000 nodes compared to 52 000, with $\Delta x_s/c = 0.0025$) show the same results, although the rate of damping is reduced. This suggests that the numerical dissipation (while necessary for accommodating shocks) is corrupting the solution when very close to the stability boundary. At $M = 0.78$ and $M = 0.79$ the URANS approach also gives steady solutions at higher values of α, consistent with the upper branch on the stability boundary. The predicted growth rate at $M = 0.79$, $\alpha = 3.0$ (where the URANS result is steady) is 0.015.

An effort to identify additional unstable modes at lower α showed nothing that could explain the difference with the experiment at $M = 0.8$. Since the URANS approach and the stability theory are in general agreement regarding the initial onset of unsteadiness, the discrepancy with the experiment is likely the result of deficiencies in the calculated steady flow, affecting both the stability and the URANS approach (e.g. from turbulence modelling) or deficiencies in the experiment (e.g. from tunnel unsteadiness or blockage effects). Independent of the differences with the experiment at $M = 0.8$, the exact values for the predicted buffet boundary depend on the turbulence model. This is similar to the post-buffet analysis, which shows some dependence on the choice of turbulence model (Thiery & Coustols 2006). However, as discussed in § 3, the better models yield consistent results.

We now examine characteristics of the separated flow at and around the buffet-onset condition. Figure 4 shows the steady-state skin-friction coefficient downstream

of the shock for three different free-stream Mach numbers. In each case, the solid line corresponds to an angle of attack just below the predicted buffet onset, and the dashed line is for an angle of attack just above the predicted buffet onset – thus bounding the onset condition. For $M = 0.76$ (figure 4*b*), the pre-buffet flow exhibits a separation bubble starting at the foot of the shock, which is near to 'bursting'. This behaviour is roughly in agreement with the idea that buffet onset occurs once the separation bubble extends from the shock to the trailing edge (Pearcey 1958; Pearcey & Holder 1962). However, for $M = 0.72$ (figure 4*a*) the steady flow exhibits a bubble both before and after the predicted buffet-onset condition – showing no link between bubble 'bursting' and buffet onset. Meanwhile, for $M = 0.8$ (figure 4*c*) the flow is separated from the foot of the shock both before and after the predicted buffet-onset condition. The experiments show buffet onset at $\alpha \approx 1^\circ$ for $M = 0.80$ (see figure 3). The steady RANS solution shows attached flow at the trailing edge for $\alpha \approx 1^\circ$. Overall, the results for the NACA0012 aerofoil do not show a clear link between buffet onset and the qualitative features of the flow separation.

5. Buffeting flow

At buffet onset, the shock begins to oscillate fore and aft (McDevitt & Okuno 1985; Lee 1990; Bartels & Edwards 1997; Jacquin *et al.* 2005). Meanwhile, the boundary layer downstream of the shock exhibits periodic thickening and thinning, which are phase locked to the shock motion. The velocity component of the global instability (u' in (5)) exhibits this exact behaviour – although its applicability is limited to small amplitudes. Figure 5 shows eight snapshots of the corresponding unsteady pressure for the unstable flow at $M = 0.76$, $\alpha = 3.2$. The pressure fluctuation appears to originate near the base of the shock. The pressure perturbation moves upward along the shock until reaching the top of the sonic zone. It then moves forward becoming ingested into the zone of sonic flow. As the pressure perturbation moves upward along the shock, it also moves aft – intensifying as it approaches the trailing edge. The pressure wave goes around the trailing edge and then propagates forward along the lower surface. The pressure fluctuation is relatively weak at the leading edge at which it experiences a significant phase shift before being ingested into the sonic zone. This unsteady flow structure is also seen in the URANS simulation for $M = 0.76$, $\alpha = 3.25$, where the peak-to-peak shock motion is $\Delta x_{shock}/c \approx 0.1$ (see figure 6). This behaviour is qualitatively different from the working model proposed by Lee (1990). In that model, buffet was assumed to result from a feedback cycle between the shock and the trailing edge; pressure waves generated at the shock propagate downstream inside the boundary layer and are scattered at the trailing edge, resulting in upstream-propagating waves outside the boundary layer – when these waves impact the shock they generate new waves starting a new cycle.

Figure 6 shows the variation of the peak-to-peak amplitude of the shock oscillation $\Delta x_{shock}/c$ and the surface pressure fluctuation p'/p_0 at $x/c = 0.8$ as obtained from the URANS. Assuming zero amplitude at $\alpha \approx 3.02^\circ$, both of these measures of the disturbance amplitude initially increase rapidly with α. It is not possible to get unsteady solutions with URANS below $\alpha \approx 3.2^\circ$ because the relatively weak unsteadiness (very small growth rate) appears to be damped by numerical dissipation. At higher angles of attack the fluctuation amplitude appears to saturate. This behaviour is in general agreement with the experiment of McDevitt & Okuno (1985), which shows rapidly increasing p' amplitude with α, followed by an amplitude saturation. The large square on figure 6 shows an estimate for the p' amplitude

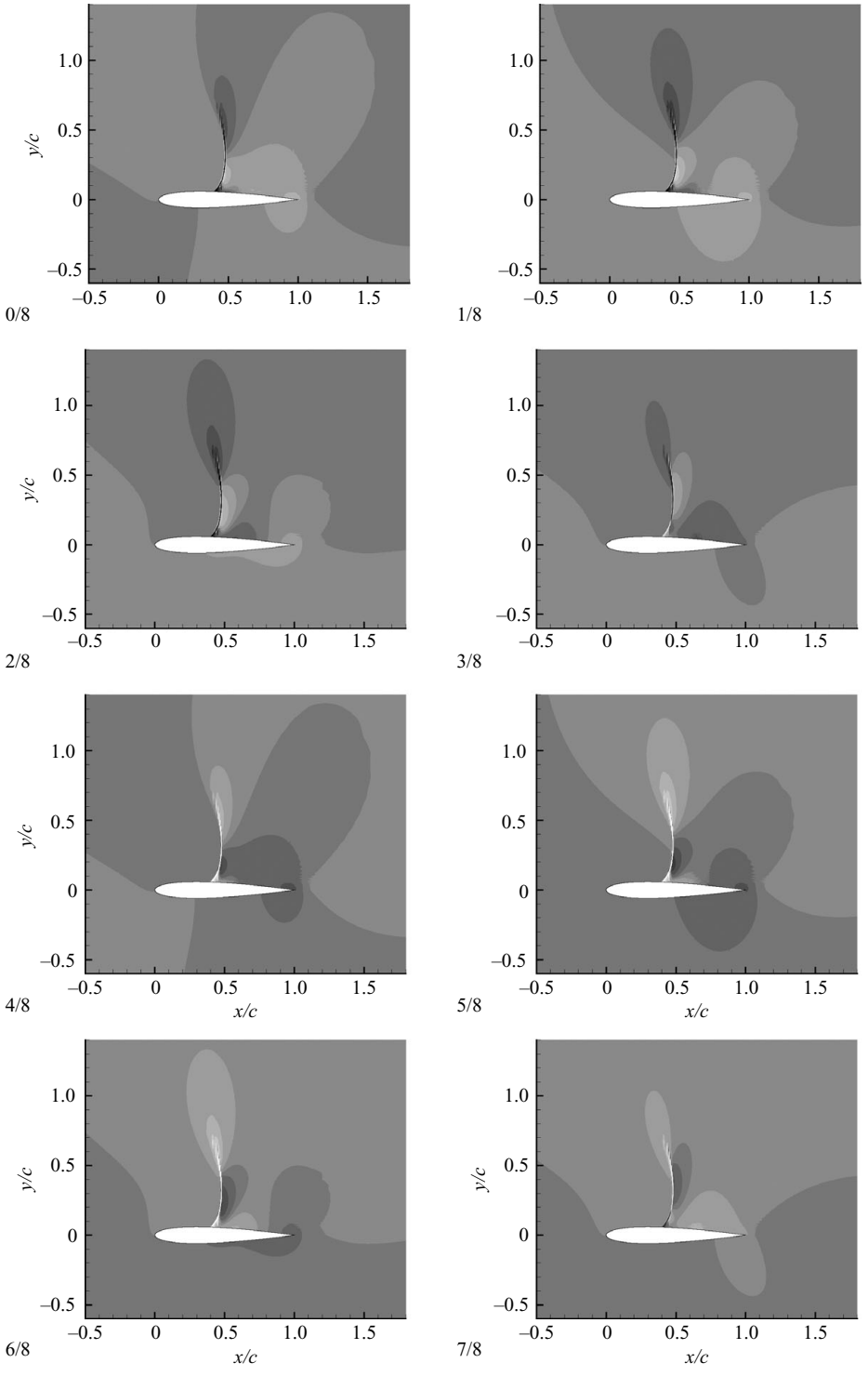

FIGURE 5. Contours of the pressure fluctuation at eight steps during the oscillation cycle, $t/T = 0,\ 1/8,\ 2/8,\ 3/8,\ 4/8,\ 5/8,\ 6/8,\ 7/8$, for the conditions $M = 0.76$, $\alpha = 3.2°$, $Re = 10^7$.

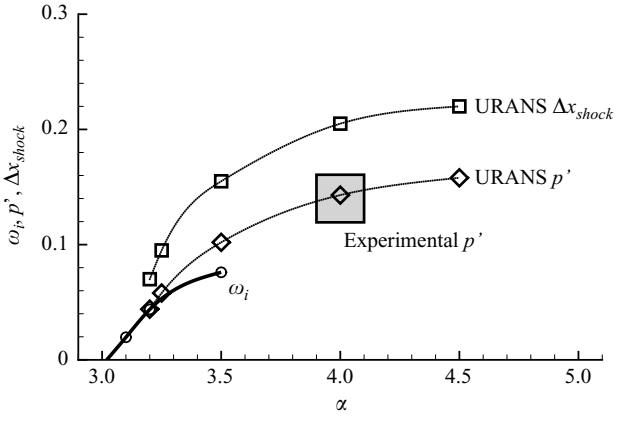

FIGURE 6. Variation of URANS peak-to-peak amplitudes Δx_{shock} and p'/p_0 with aerofoil angle of attack for $M = 0.76$, $Re = 10^7$. Also shown is the instability growth rate and the p'/p_0 observed in the experiments of McDevitt & Okuno (1985).

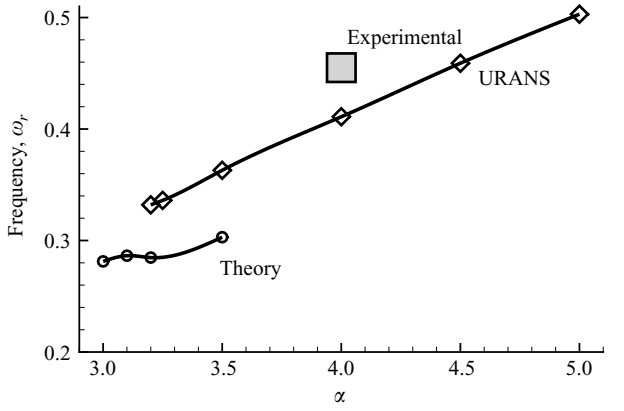

FIGURE 7. Variation of frequency with aerofoil angle of attack for $M = 0.76$, $Re = 10^7$. The experimental value is from McDevitt & Okuno (1985).

taken from the experiment at a slightly higher Mach number $M \approx 0.77$. Near buffet onset, the instability growth rate also exhibits near-linear variation with the angle of attack. Thus, the amplitude variation near the critical conditions is consistent with a supercritical bifurcation from a weakly nonlinear theory (Drazin & Reid 1981).

Figure 7 shows the variation of the buffeting frequency as the angle of attack increases. Near buffet onset $\alpha \approx 3.2^\circ$, the URANS result is within 15 % of the global-stability result. Simulations with different grids show negligible change in the frequency, unlike the growth/decay characteristics. The differences are attributed to nonlinear effects in the URANS approach; a linear extrapolation of the URANS results down to $\alpha = 3.02^\circ$ reduces the frequency difference to less than 10 %. As α is increased, the stability theory shows a weak variation in frequency with α. By contrast, the URANS frequency rises by 50 % over 1.5° of α variation. The large symbol shows an estimate for the experimental frequency for these conditions – in general agreement with the URANS approach. The significant rise in the URANS frequency while the instability frequency is nearly constant is similar to the frequency

variation for the early vortex shedding on a circular cylinder with increasing Reynolds number (see, for example, CGM).

6. Conclusions

Buffet onset is analysed following the global-stability formulation of CGM and the URANS numerical-simulation approach as implemented in the NTS code (Strelets 2001). The analysis shows the origin of buffet onset is tied to a global instability. The buffeting flow in the neighbourhood of the onset condition is consistent with a supercritical Hopf bifurcation. Global-stability analysis provides good qualitative and quantitative descriptors for buffet onset. The method provides better predictive capability than earlier empirical and heuristic models, which are currently in use.

REFERENCES

Bartels, R. E. & Edwards, J. W. 1997 Cryogenic tunnel pressure measurements on a supercritical airfoil for several shock buffet conditions. *Tech Memo*. 110272. NASA.

Bigarella, E. D. V. & Azevedo, J. L. F. 2007 Advanced eddy-viscosity and Reynolds-stress turbulence model simulations of aerospace applications. *AIAA J*. **45** (10), 2369–2390.

Catalano, P. & Amato, M. 2003 An evaluation of RANS turbulence modelling for aerodynamic applications. *Aerosp. Sci. Technol*. **7** (7), 493–509.

Crouch, J. D., Garbaruk, A. & Magidov, D. 2007 Predicting the onset of flow unsteadiness based on global instability. *J. Comput. Phys*. **224**, 924–940.

Crouch, J. D., Garbaruk, A., Magidov, D. & Jacquin, L. (2009) Global structure of buffeting flow on transonic airfoils. In *IUTAM Symposium on Unsteady Separated Flows and Their Control* (ed. M. Braza & K. Hourigan), Springer. Submitted.

Drazin, P. G. & Reid, W. H. 1981 *Hydrodynamic Stability*. Cambridge University Press.

Garbaruk, A., Shur, M., Strelets, M. & Spalart, P. R. 2003 Numerical study of wind-tunnel walls effects on transonic airfoil flow. *AIAA J*. **41** (6), 1046–1054.

Israel, D. M. 2006 URANS and VLES: using conventional RANS models for time dependent flows. *Paper* 2006-3908. AIAA.

Jacquin, L., Molton, P., Deck, S., Maury, B. & Soulevant, D. 2005 An experimental study of shock oscillation over a transonic supercritical profile. *Paper* 2005-4902. AIAA.

Lee, B. H. K. 1990 Oscillatory shock motion caused by transonic shock boundary-layer interaction. *AIAA J*. **28**, 942–944.

Lee, B. H. K. 2001 Self-sustained shock oscillation on airfoils at transonic speeds. *Prog. Aero. Sci*. **37**, 147–196.

Lehoucq, R. B., Sorensen, D. C. & Yang, C. 1998 *ARPACK User's Guide*. SIAM.

Mabey, D. G., Welsh, B. L. & Cripps, B. E. 1981 Periodic flows on a rigid 14 % thick biconvex wing at transonic speeds. *Tech Rep*. 81059. Royal Aircraft Establishment.

McDevitt, J. B. & Okuno, A. F. 1985 Static and dynamic pressure measurements on a NACA0012 airfoil in the Ames high Reynolds number facility. *Tech Paper* 2485. NASA.

Menter, F. R. 1994 Two-equation eddy-viscosity turbulence models for engineering applications. *AIAA J*. **32** (8), 1598–1605.

Pearcey, H. H. 1958 A method for the prediction of the onset of buffeting and other separation effects from wind tunnel tests on rigid models. *Report* 223. AGARD.

Pearcey, H. H. & Holder, D. W. 1962 Simple methods for the prediction of wing buffeting resulting from bubble type separation. *Aero Rep*. 1024. National Physical Laboratory.

Roe, P. L. 1981 Approximate Rieman solvers, parameters vectors and difference schemes. *J. Comput. Phys*. **43**, 357–372.

Shur, M. L., Spalart, P. S., Squires, K. D., Strelets, M. Kh. & Travin, A. 2005 Three dimensionality in Reynolds-averaged Navier–Stokes solutions around two-dimensional geometries. *AIAA J*. **43** (6), 1230–1242.

Spalart, P. R. 2000 Trends in Turbulence Treatments. *Paper* 2000-2306. AIAA.

Spalart, P. R. & Allmaras, S. R. 1994 A one-equation turbulence model for aerodynamic flows. *Rech. Aérosp.*. (1), 5–21. Also *Paper* 92-0439. AIAA.

Strelets, M. 2001 Detached-eddy simulation of massively separated flows. *Paper* 2001-0879. AIAA.

Theofilis, V. 2003 Advances in global linear instability analysis of nonparallel and three-dimensional flows. *Prog. Aero. Sci.*, **39**, 249–315.

Thiery, M. & Coustols, E. 2006 Numerical prediction of shock induced oscillations over a two-dimensional airfoil: influence of turbulence modelling and test section walls. *Intl J. Heat Fluid Flow*. **27**, 661–670.